JGR Atmospheres

RESEARCH ARTICLE
10.1029/2025JD044106

Sensitivity of Coastal Rainfall Simulation to the Assimilation of Wind Profiles Near the Marine Boundary Layer Jet: An Observing System Simulation Experiment

Yican Lin[1] and **Yu Du**[1,2,3]

[1]School of Atmospheric Sciences, Sun Yat-sen University, and Southern Marine Science and Engineering Guangdong Laboratory (Zhuhai), Zhuhai, China, [2]Guangdong Province Key Laboratory for Climate Change and Natural Disaster Studies, Sun Yat-sen University, Zhuhai, China, [3]Key Laboratory of Tropical Atmosphere-Ocean System, Sun Yat-sen University, Ministry of Education, Zhuhai, China

Key Points:

- Coastal heavy rainfall simulations are sensitive to variations in the boundary layer jet (BLJ) over the South China Sea
- Assimilating wind profile observations from different oceanic locations leads to varying impacts on rainfall simulation accuracy
- Wind profile assimilation modifies the dynamic and thermodynamic effects of the BLJ, influencing precipitation development

Correspondence to:
Y. Du,
duyu7@mail.sysu.edu.cn

Citation:
Lin, Y., & Du, Y. (2025). Sensitivity of coastal rainfall simulation to the assimilation of wind profiles near the marine boundary layer jet: An observing system simulation experiment. *Journal of Geophysical Research: Atmospheres*, *130*, e2025JD044106. https://doi.org/10.1029/2025JD044106

Received 12 APR 2025
Accepted 21 JUL 2025

Author Contributions:
Conceptualization: Yu Du
Data curation: Yican Lin
Formal analysis: Yican Lin
Funding acquisition: Yu Du
Methodology: Yican Lin
Project administration: Yu Du
Resources: Yu Du
Software: Yican Lin
Supervision: Yu Du
Validation: Yican Lin
Visualization: Yican Lin
Writing – original draft: Yican Lin
Writing – review & editing: Yican Lin

Abstract An Observing System Simulation Experiment was conducted to assess the impact of assimilating oceanic wind profiles on the simulations of warm-sector heavy rainfall along the South China coast. This rainfall event was strongly influenced by an upstream boundary layer jet (BLJ) over the northern South China Sea (NSCS). Using a 21-member WRF ensemble initialized with Global Ensemble Forecast System data, the best-performing member was selected as the nature run. Simulated wind profiles over the NSCS from the nature run were assimilated into the worst-performing member at the initial time step, improving the representation of the BLJ structure and strength. The data assimilation experiments reveal a significant sensitivity of simulated rainfall intensity and spatial distribution to both the number and location of assimilated wind profile observations. A strengthened marine BLJ with a more southerly wind component extending toward the coast enhanced low-level convergence, upward motion, and moisture transport at its terminus, thus creating a more favorable environment for convection. However, momentum budget analysis indicates that, despite wind profile assimilation, the nearshore BLJ remained too weak to sustain upscale convective growth following convective initiation.

Plain Language Summary Coastal heavy rainfall can cause flooding and disrupt daily life. A key driver of these storms is a boundary layer jet (BLJ)—a strong low-level wind over the ocean that carries moisture inland. However, predicting how these winds interact with storms remains challenging due to limited ocean-based observations. To address this, we conducted simulation experiments to test how adding artificial wind data over the northern South China Sea could improve coastal rainfall forecasts. Our results show that assimilating wind data from different locations improved the early stages of the storm development, but challenges remained in capturing the later development of organized heavy rainfall. While the BLJ initially strengthened, it was still too weak to fully support the growth of the storm. These findings underscore the importance of collecting more ocean-based wind data to enhance forecast accuracy. However, improving heavy rainfall prediction also requires a deeper understanding of how other atmospheric processes interact with these winds to influence storm evolution.

1. Introduction

In South China, nearly half of the annual precipitation occurs during the pre-summer rainy season (April–June), the first rainy season on the Chinese mainland (Ding, 1994). During this season, frequent and intense heavy rainfall events can cause severe natural disasters, such as floods and debris flows, leading to significant economic and societal losses (Y. Luo et al., 2017). The rainfall during this season primarily falls into two categories: frontal rainfall (FR) and warm-sector rainfall (WR).

FR typically develops near synoptic fronts, where cold and dry airflows from the north converge with warm and moist airflows from the south (Ding, 1994; S. Zhao et al., 2007), and is strongly influenced by synoptic-scale dynamic forcing, particularly front lifting (Tao & Chen, 1987). In contrast, WR occurs approximately 200–300 km from the frontal systems (Ding, 1994; S. Huang et al., 1986; Y. Luo et al., 2017), and is affected by various mesoscale and local factors, including convergence associated with low-level jets (LLJs) (Du, Chen, Han, Bai & Li, 2020; Du & Chen, 2018, 2019; M. Zhang & Meng, 2019), land-sea thermal contrast (X. Chen et al., 2016; Gao et al., 2022), cold pools (S. Zhao et al., 2007), complex terrain (Bai et al., 2021), and gravity

waves (Yang et al., 2024). Due to the complex and unpredictable interactions of these factors, WR frequently develops suddenly, resulting in relatively poor quantitative precipitation forecast (QPF) skill and limited predictability.

LLJs can be classified into synoptic-system-related LLJs (SLLJs) and boundary layer jets (BLJs) (Du & Chen, 2019; Du et al., 2014). SLLJs typically form in the lower free troposphere and are associated with synoptic-scale weather systems, whereas BLJs develop within the boundary layer, characterized by strong vertical shear and a pronounced diurnal cycle, with maximum wind speeds occurring at night (Du & Chen, 2018, 2019; X. Zhang et al., 2024). Both SLLJs and BLJs are crucial in triggering and enhancing rainfall by providing favorable dynamic and thermodynamic conditions (G. Chen et al., 2017; Du et al., 2022; Du & Chen, 2019; Y. Luo & Du, 2023; Yang et al., 2025). These jets contribute to strong ascending motion due to low-level convergence at their terminus. They also transport large amounts of warm moist air, creating a humid and unstable environment conducive to deep convection (Y. Luo & Du, 2025).

In South China, statistical studies have shown a strong correlation between LLJs and heavy rainfall events (X. Li & Du, 2021). The coupling of BLJs over the ocean and SLLJs over the land plays a critical role in the development of WR in South China (Du & Chen, 2018, 2019). Marine BLJs, in particular, are closely associated with coastal rainfall through various mechanisms, including interactions with coastal terrain (G. Chen et al., 2017; Du, Chen, Han, Bai & Li, 2020; Du, Chen, Han, Mai, et al., 2020; Du & Chen, 2019), the land-sea thermal contrast (G. Chen et al., 2017; Wu et al., 2020), and the differential friction of the underlying surface (G. Chen et al., 2017; Du, Chen, Han, Bai & Li, 2020; Du, Chen, Han, Mai, et al., 2020; Z. Li et al., 2020; M. Zhang & Meng, 2019). The spatial structure and temporal evolution of marine BLJs are essential for the initiation and development of WR (Du & Chen, 2018, 2019; Du et al., 2022). Moreover, the diurnal variation in BLJs influences the diurnal pattern of coastal rainfall (Dong et al., 2021).

Given the critical role of marine BLJs in WR over South China and the scarcity of observations for these jets, improving WR forecast accuracy remains a significant scientific challenge. Shen and Du (2023) demonstrated that WR forecasts are highly sensitive to the strength and direction of BLJs when varying boundary layer schemes are applied. Previous studies have focused on assimilating wind field data, such as Doppler radars, surface, and sounding data over land, to improve heavy rainfall forecasts (Ha et al., 2011; Hou et al., 2015; Sun et al., 2020). However, limited research has examined using wind profile observations over the ocean to generate more accurate analysis fields, enabling BLJs over the South China Sea (SCS) to better align with actual observations. The severe lack of boundary layer wind observations over the SCS present a key challenge. To address this gap, an Observing System Simulation Experiment (OSSE) provides an effective approach for assessing potential improvements in WR forecasting by incorporating a more accurate analysis field, even in the absence of real observations.

An OSSE consists of a nature run (i.e., an approximation of the real atmosphere), simulated observations, and data assimilation (DA) experiments. These experiments are designed to evaluate the impact of the simulated observations. The nature run is typically derived from a high-resolution, state-of-the-art model forecast, which serves both as a basis for generating simulated observations and as a benchmark for validating DA experiments (S.-H. Chen et al., 2011). OSSEs have been widely applied in various research areas, such as assessing the impact of future satellite observations on numerical weather prediction (Masutani et al., 2010), evaluating the influence of different observational strategies on both analysis and short-term forecasts in field experiments (S.-H. Chen et al., 2011), investigating the joint assimilation of radar network and ground-based profiling platform data for convective storm forecasting (Huo et al., 2023) and the assimilation of vertical wind measurements from various radar wind profiler network layouts to improve convective-scale forecasts (J. Zhao et al., 2024). Beyond these applications, OSSEs present a promising tool for assessing the impact of assimilating wind profile observations near BLJs over the SCS on WR forecasts in South China.

Du, Chen, Han, Bai, and Li (2020) studied a warm-sector heavy rainfall event that occurred along the coast of South China on 21–22 June 2018. Their study revealed that coastal convection initiation (CI) and its subsequent upscale convective growth (UCG) in this warm-sector heavy rainfall event were primarily driven by the dynamic and thermodynamic effects of the marine BLJ in convection-permitting simulations. CI and subsequent UCG near the coast occurred downstream of a southwesterly BLJ over the SCS, demonstrating that the spatial structure and temporal variation of the BLJ exerted a significant influence on CI and UCG by driving mesoscale ascent and low-level moistening near the south coast of China.

In this study, we conducted a high-resolution ensemble simulation and developed an OSSE framework based on the warm-sector heavy rainfall event described above. Our primary goal is to address the following key scientific questions.

1. Does assimilating wind profile data over the SCS improve the forecast of the warm-sector heavy rainfall in the coastal region of South China?
2. Does the assimilation of wind profile data from different locations over the SCS have varying impacts on forecast improvements?
3. What are the underlying mechanisms by which assimilating wind profile data associated with BLJ over the SCS improves the forecasts of the warm-sector heavy rainfall?

By answering these questions, we aim to provide valuable insights for future field campaigns and observational strategies over the SCS, ultimately improving WR forecasting in South China. The remainder of this paper is structured as follows: Section 2 details the numerical model and data sets used in this study. Section 3 provides an overview of the heavy rainfall event and describes the OSSE design. Section 4 presents the OSSE results and explores the underlying mechanisms. Finally, Section 5 summarizes the key findings and conclusions.

2. Data and Method

2.1. Data

The Climate Prediction Center morphing technique (CMORPH) rainfall data, with a spatial resolution of 8 km and a temporal resolution of 30 min, was used to represent the observed accumulated precipitation (Xie et al., 2019).

The ERA5 reanalysis data set, produced by the European Center for Medium-Range Weather Forecasts (ECMWF), was utilized to provide the synoptic background for heavy rainfall. This data set offers a wind field with a horizontal resolution of $0.25° \times 0.25°$ and an hourly temporal resolution (Hersbach et al., 2018).

The ensemble simulation was initialized with the Global Ensemble Forecast System (GEFS) data (Toth & Kalnay, 1993). The GEFS consists of 21 separate forecasts conducted by the National Centers for Environmental Prediction (NCEP). These forecasts are initialized using the Ensemble Transform with Rescaling (ETR) method (Wei et al., 2008) and the Stochastic Total Tendency Perturbation (STTP) technique, which together ensure a diverse range of ensemble member simulations.

2.2. Numerical Model and Data Assimilation System

In this study, we employed the Advanced Research version of the Weather Research and Forecasting Model (WRF-ARW; version 4.5.1; Skamarock et al., 2019). The model domain configuration is shown in Figure 1a: the inner domain (d02) has a horizontal grid spacing of 4 km, and it is one-way nested within an outer domain (d01) with a horizontal grid spacing of 12 km. The model employs a vertically stretched grid with 51 levels to better capture the atmospheric boundary layer.

The ensemble simulation was initialized from the 1200 UTC 21 June 2018 using GEFS data, with lateral boundary condition updated every 6 hr. The Kain–Fritsch convection parameterization (Kain, 2004) was used in d01 while it was turned off in d02. Both domains implemented the following schemes: the Thompson et al. (2008) bulk microphysics scheme, the YSU boundary layer scheme (Hong et al., 2006), the Rapid Radiative Transfer Model for Global Climate Models (RRTMG) longwave and shortwave radiation schemes (Iacono et al., 2008), the revised MM5 Monin–Obukhov surface-layer scheme (Jiménez et al., 2012), and the unified Noah land surface model (Livneh et al., 2011).

Data assimilation was conducted using the WRF three-dimensional variational data assimilation (WRF-3DVAR) system (Barker et al., 2004a, 2004b) within the framework of the OSSE. The WRF–3DVAR system adopts a multivariate incremental formulation (Courtier et al., 1994), where the preconditioned control variables are stream function, velocity potential, unbalanced pressure, and total water mixing ratio. The aim of the three-dimensional variational approach is to find the best compromise between a priori estimates of the analysis field and the observations through an iterative solution that minimizes the cost function:

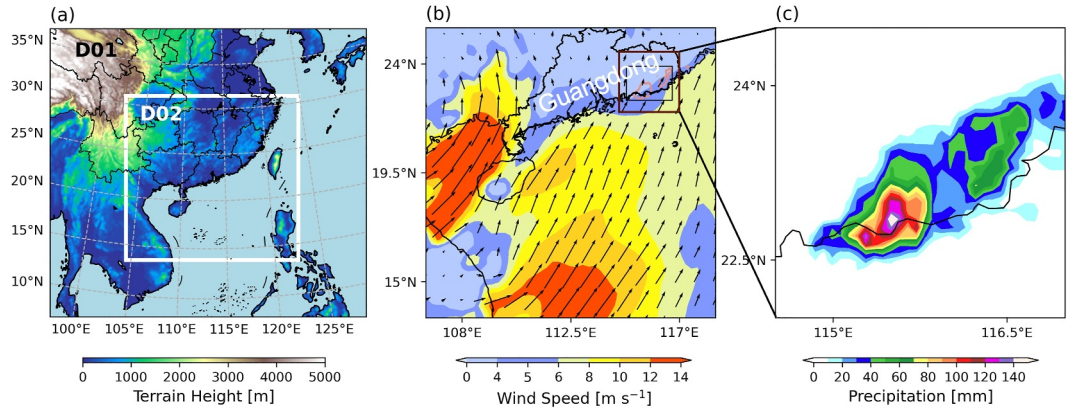

Figure 1. (a) Domain configurations of D01 and D02 with terrain height (shaded). (b) Horizontal wind speed (shaded) and wind vectors at 950 hPa, averaged from 18:00 UTC 21 June to 00:00 UTC 22 June, derived from ERA5. The orange contour represents the 6-hr accumulated precipitation of 50 mm during the same period. The black box indicates the core precipitation area. (c) Spatial distribution of 6-hr accumulated precipitation (shaded) within the brown box region in panel (b) derived from CMORPH.

$$J(x) = J^{\mathrm{b}} + J^{\circ} = \frac{1}{2}\left\{[y^{\circ} - H(x)]^{T}\mathbf{R}^{-1}[y^{\circ} - H(x)] + \left(x - x^{\mathrm{b}}\right)^{T}\mathbf{B}^{-1}\left(x - x^{\mathrm{b}}\right)\right\}, \quad (1)$$

where superscript "b" denotes the background field and superscript "o" denotes the observation field; x^b is a priori state (background), y° is the observation, and H is the operator that converts the model state to the observation space. The cost function J measures the discrepancy between the field x and both the observations y° and the background x^b, scaled by the observation error covariance matrix $\boldsymbol{R}$ and background error covariance matrix $\boldsymbol{B}$. For a detailed description of the 3DVAR system, refer to Barker et al. (2003, 2004a, 2004b).

2.3. Threat Score

To quantitatively evaluate the performance of each ensemble forecast member, the threat sore (TS) was calculated for different thresholds of accumulated precipitation. The TS is defined as

$$\mathrm{TS} = \frac{H}{H + M + F}, \quad (2)$$

where H (Hits) is the number of grid points where both forecast and observation exceed the rainfall threshold, M (Misses) is the number of grid points where the observation exceeds the threshold but the forecast does not, and F (False Alarms) is the number of grid points where the forecast exceeds the threshold but the observation does not (Wilks, 1995). This score quantifies the accuracy of the model's predicted precipitation relative to observations. Since the spatial resolution of the numerical simulation is higher than that of the CMORPH data, the model outputs were interpolated onto the CMORPH grid prior to the TS calculation to ensure consistency.

2.4. Moisture Budget Equation

Following Du, Chen, Han, Bai, and Li (2020), the contributions to the increase in the water vapor mixing ratio (q_v) are quantitatively diagnosed using the following equation:

$$\underbrace{\frac{\partial q_v}{\partial t}}_{\mathrm{TD}} = \underbrace{-\boldsymbol{V}_{\mathrm{h}} \cdot \nabla_{\mathrm{h}} q_v}_{\mathrm{HAD}} \underbrace{-\omega \frac{\partial q_v}{\partial p}}_{\mathrm{VAD}} \underbrace{+R}_{\mathrm{Residual}}, \quad (3)$$

where $\partial q_v/\partial t$ represents the local change in q_v, $-\boldsymbol{V}_{\mathrm{h}} \cdot \nabla_{\mathrm{h}} q_v$ and $-\omega\left(\partial q_v/\partial p\right)$ are horizontal and vertical transport terms ($\boldsymbol{V}_{\mathrm{h}}$ is the horizontal wind vector and ω is the vertical velocity hereafter), respectively, and R represents the

residual term that accounts for other contributions. To compute $\partial q_v/\partial t$, an hourly centered time difference approach is used: $(\partial q_v/\partial t)_{t_0} = (q_{v_{t_0+\Delta t}} - q_{v_{t_0-\Delta t}})/2\Delta t$, where $\Delta t = 1$ hr. Similarly, for the vertical transport term $(\partial q_v/\partial \mathrm{p})_{p_0} = (q_{v_{p_0+\Delta p}} - q_{v_{p_0-\Delta p}})/2\Delta p$. In this study, the focus is on the 950-hPa level, with $\Delta p = 50$ hPa, which approximately corresponds to the vertical distance between two neighboring model levels. The residual term R is calculated as: $\partial q_v/\partial t + \mathbf{V}_h \cdot \nabla_h q_v + \omega(\partial q_v/\partial p)$. In practice, R includes contributions from subgrid mixing (vertical turbulence mixing) in the boundary layer, condensation/evaporation processes, and computational errors (e.g., interpolation errors due to complex coastal terrain).

2.5. Momentum Budget Equation

Following Du et al. (2014, 2015) and Zeng et al. (2019), the momentum budget equation can be expressed as

$$\underbrace{\frac{\partial \boldsymbol{V}}{\partial t}}_{\mathrm{TD}} = \underbrace{-\boldsymbol{V}_{\mathrm{h}} \cdot \nabla_{\mathrm{h}} \boldsymbol{V}}_{\mathrm{HAD}} \underbrace{-\omega \frac{\partial \boldsymbol{V}}{\partial p}}_{\mathrm{VAD}} \underbrace{-\nabla \varphi}_{\mathrm{PGF}} \underbrace{-f\boldsymbol{k} \times \boldsymbol{V}}_{\mathrm{CF}} \underbrace{+\boldsymbol{F}_{\mathbf{r}}}_{\mathrm{Fr}}, \tag{4}$$

where $\partial \mathbf{V}/\partial t$ represents the tendency of winds ($\mathbf{V}$ denotes the three-dimensional wind vector, but only the meridional wind component is considered in this study), $-\boldsymbol{V}_{\mathrm{h}} \cdot \nabla_{\mathrm{h}} \mathbf{V}$ and $-\omega(\partial \mathbf{V}/\partial p)$ are horizontal and vertical advection terms, respectively, $-\nabla\varphi$ is the pressure gradient force (PGF) term (φ is the geopotential), $-f\boldsymbol{k} \times \boldsymbol{V}$ is the Coriolis force (CF) term (f is the Coriolis parameter, $\boldsymbol{k}$ is the unit vector in the vertical direction, perpendicular to the horizontal plane), and friction force (Fr) is calculated as the residual of the other terms: $\partial \mathbf{V}/\partial t + \boldsymbol{V}_{\mathrm{h}} \cdot \nabla_{\mathrm{h}} \mathbf{V} + \omega(\partial \mathbf{V}/\partial p) + \nabla\varphi + f\boldsymbol{k} \times \boldsymbol{V}$.

3. Case Overview and Experimental Design

On 21–22 June 2018, a warm-sector heavy rainfall event occurred along the South China coast, producing over 50 mm of accumulated precipitation within 6 hr. According to Du, Chen, Han, Mai, et al. (2020) and Du, Chen, Han, Bai, and Li (2020), a deep southwest–northeast-oriented trough at 500 hPa was present over northern China, while a low-pressure vortex at 850 hPa was centered over southwestern China, accompanied by a west–east-oriented shear line at 925 hPa. While these large-scale features provided the broader synoptic background, they did not directly trigger the coastal heavy rainfall. The core of the rainfall, as depicted in Figure 1c, was concentrated near the coastline and exhibited a pronounced linear-shape structure. This rainfall pattern was closely associated with a southwesterly BLJ over the northern South China Sea (NSCS). Upstream of the rainfall region, strong southwesterly winds at 950 hPa (>8 m s^{-1}, indicated by the bright yellow shading) prevailed, characterizing the marine BLJ, which played a crucial role in modulating moisture transport and initiating convection (Figure 1b).

To design an OSSE, we conducted a 21-member ensemble simulation initialized with the GEFS data. The 6-hr accumulated precipitation from 18:00 UTC 21 June to 00:00 UTC 22 June was analyzed (Figure 2). Among the ensemble members, mem03 exhibited no precipitation (Figure 2d) and was selected as "Bad" member, serving as the control run without data assimilation. To identify a suitable nature run, TSs for each ensemble member (Figure 3) showed that mem20 outperformed the others, except at lower precipitation thresholds (<23 mm). Moreover, mem20 exhibited a linear-shape precipitation structure along the coast, albeit slightly displaced northward compared to observations. Based on these considerations, mem20 was chosen as "Good" member and served as the nature run for the OSSE.

To investigate the impact of wind profile assimilation on the simulation of warm-sector heavy rainfall, we conducted a series of data assimilation experiments using the 3DVAR method in WRFDA. The background error covariance matrix was constructed using the generic CV3 option, which includes stream function, unbalanced velocity potential, unbalanced temperature, pseudo-relative humidity, and unbalanced surface pressure as control variables. The variance scaling factor, horizontal length scale factor, and vertical length scale factor were set to the default values of 0.25, 1.00, and 1.50, respectively, to define the spatial structure of the background error covariance matrix (Hu et al., 2017).

The simulated wind profiles, extracted from "Good" member, were designed to emulate radiosonde observations collected aboard a scientific research vessel, representing in situ, point-based vertical profiles of horizontal wind

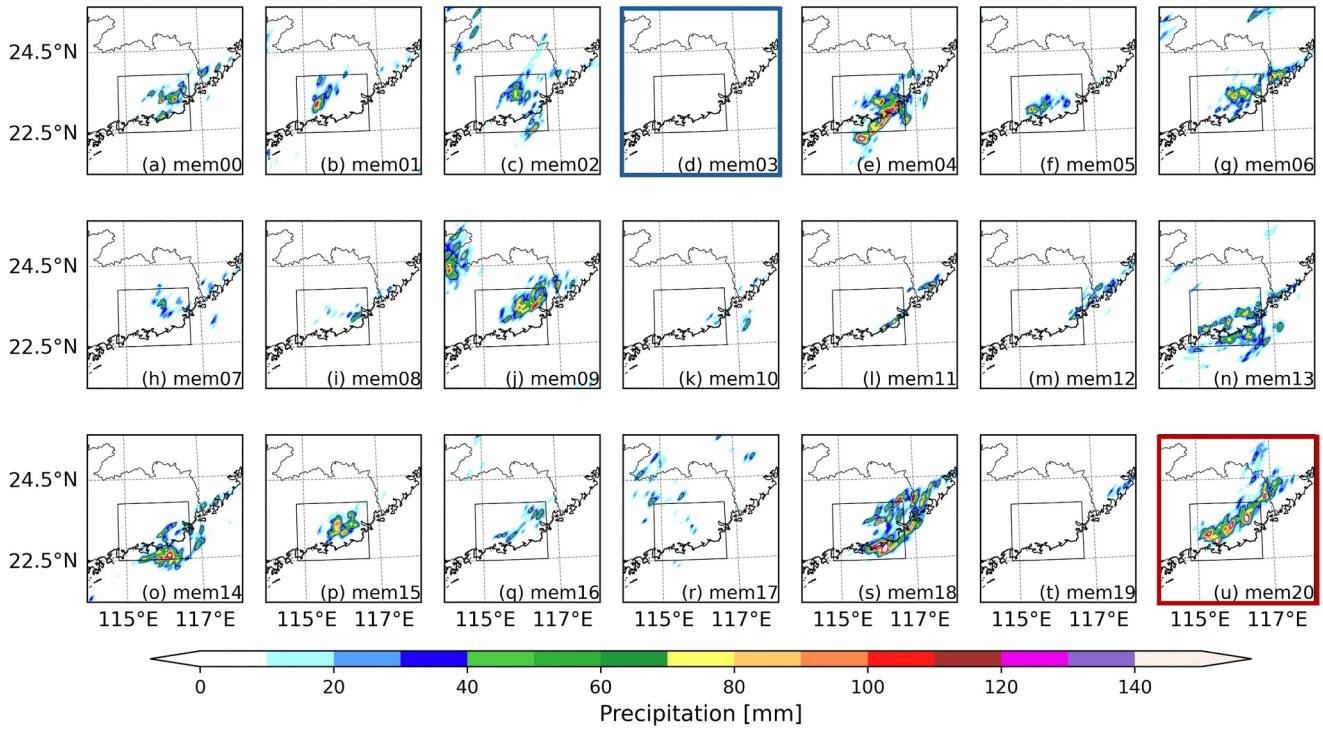

Figure 2. Six-hours accumulated precipitation (mm, shaded) for ensemble members (a) mem00 to (u) mem20 from 18:00 UTC 21 June to 00:00 UTC 22 June. The black boxes are the same as those in Figure 1. "Bad" member and "Good" member are highlighted with blue and red boxes, respectively.

speed and direction. For computational efficiency and optimization, the pseudo-observations were placed at model levels. Final observations were obtained by adding perturbations to the u/v components of the wind profiles. These perturbations were modeled as Gaussian random errors with a mean of zero and a standard deviation of 1 m s^{-1} (J. Zhao et al., 2024). The observation operator H, implemented via the "asm_sd" assimilation

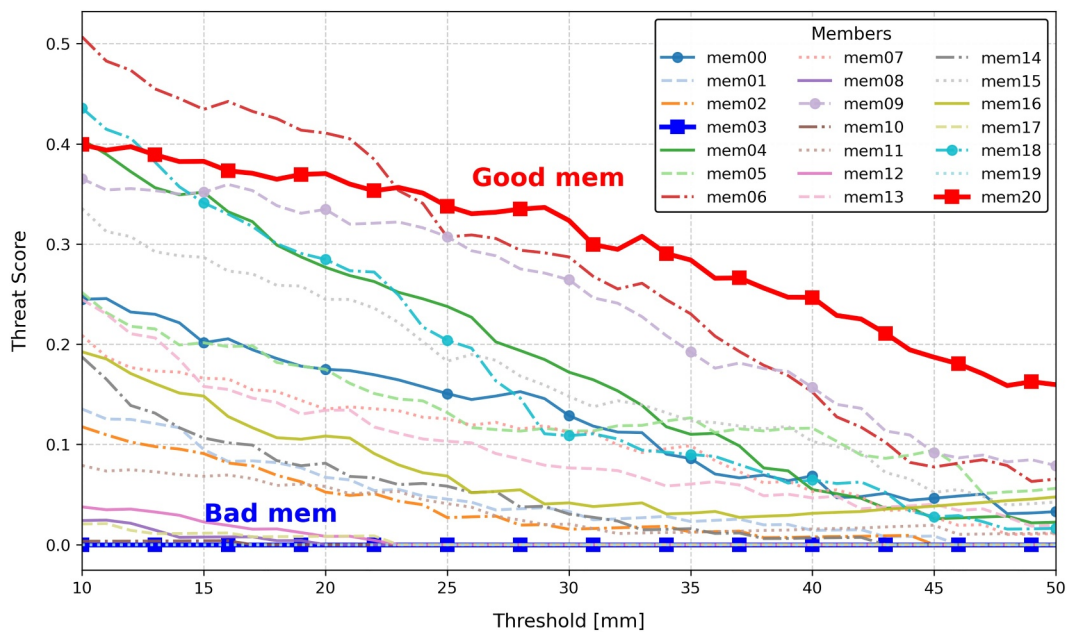

Figure 3. Comparison of threat scores of members in the ensemble simulation.

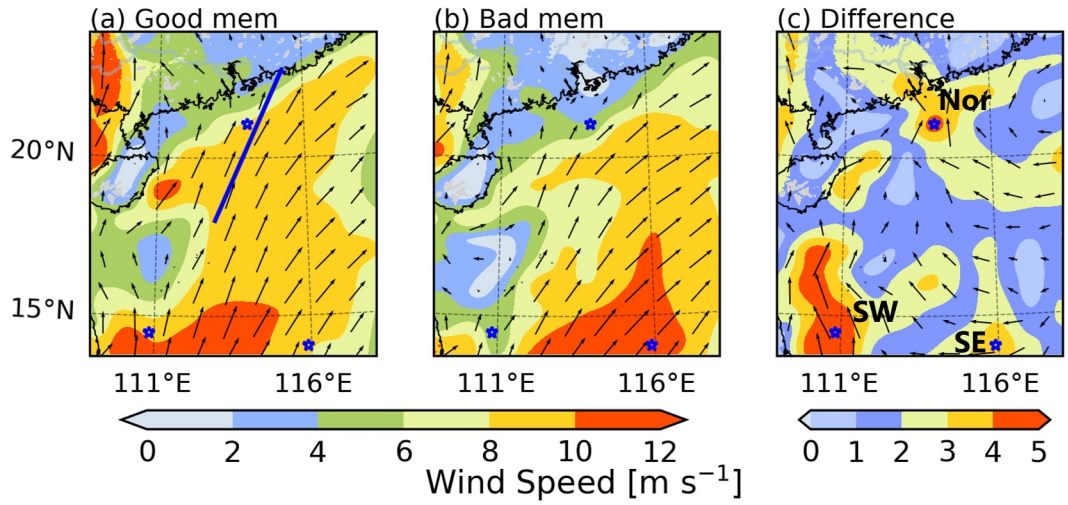

Figure 4. Horizontal distribution of wind speed (shaded) and wind vectors at 950 hPa at 12:00 UTC 21 June for (a) "Good" member, (b) "Bad" member, and (c) the difference between "Good" member and "Bad" member from the numerical simulation. In panel (c), blue stars denote the locations of the identified high-wind-deviation cores used for wind profile assimilation experiments. The blue line represents the cross-section used in Figure 10.

method (X.-Y. Huang et al., 2013), directly assimilates wind speed and direction by interpolating the model wind components—converted from u and v to speed and direction—to the observation locations.

Observation errors were assigned using the Observation Preprocessor (OBSPROC), based on the standard table of observation error values used by the U.S. Air Force Weather Agency (AFWA). Wind direction errors decrease from 20.0° at the surface to 15.0° at higher altitudes while wind speed errors range from 1.1 m s^{-1} to 3.0 m s^{-1} depending on the vertical level. These profiles were assimilated into the initial conditions of "Bad" member over domain D02 at 12:00 UTC on 21 June.

Next, we identified the optimal locations for wind profile assimilation by examining the differences in the initial 950 hPa wind fields between "Good" member and "Bad" member (Figure 4). Although both experiments exhibited a BLJ over the NSCS, notable differences were observed (Figures 4a and 4b).

1. In "Good" member, the region with wind speeds exceeding 8 m s^{-1} extended farther north compared to "Bad" member (highlighted by bright yellow shading).
2. The BLJ in "Good" member featured stronger southerly wind component, whereas "Bad" member exhibited a more pronounced westerly wind component.
3. The upstream BLJ core in "Good" member was located farther west than in "Bad" member.

These differences between the two experiments revealed three distinct high-wind-deviation cores, marked by stars in Figure 4c.

1. Northern core: Located to the north of the upstream BLJ, near the south coast of China, exhibiting stronger southerly winds in "Good" member.
2. Southwestern core: Positioned at the western flank of the upstream BLJ, also featuring enhanced southerly winds in "Good" member.
3. Southeastern core: Located at the eastern flank of the upstream BLJ, where weaker westerly winds are present in "Good" member.

Given these differences, we hypothesize that the BLJ structure at these three oceanic locations plays a key role in the contrasting precipitation characteristics between "Good" member and "Bad" member. To examine this hypothesis, we conducted four DA experiments, each assimilating wind profiles from different locations.

1. DA_Nor: Assimilates wind profiles from the northern core (21.08°N, 114.05°E).
2. DA_SW: Assimilates wind profiles from the southwestern core (14.47°N, 110.83°E).
3. DA_SE: Assimilates wind profiles from the southeastern core (14.06°N, 115.90°E).

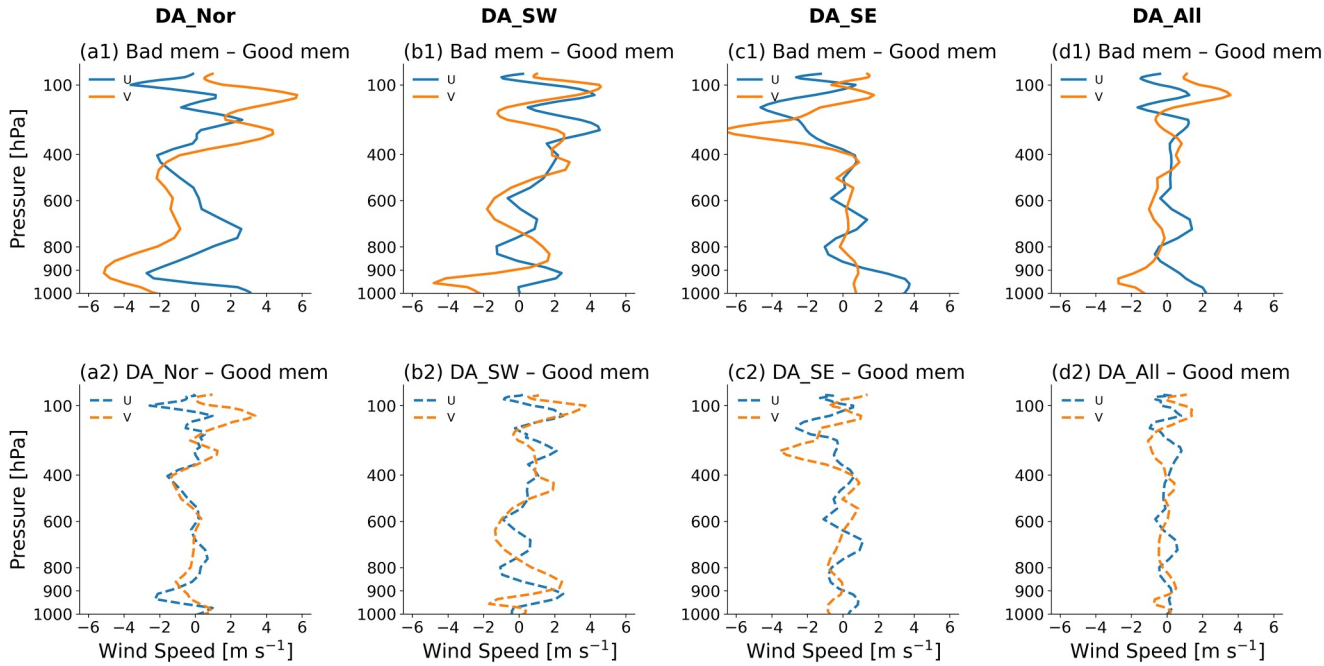

Figure 5. Wind profile differences at 12:00 UTC 21 June (a1–d1) between "Bad" member and "Good" member and (a2–d2) between DA experiments and "Good" member at the corresponding assimilated locations.

4. DA_All: Simultaneously assimilates wind profiles from all three locations.

These experiments were designed to evaluate the relative contribution of wind profile assimilation at different locations to the evolution of the marine BLJ and its downstream impact on precipitation. In this study, the simulated profiles were at full model vertical levels. To assess vertical sensitivity, an additional experiment was conducted in which only the portion of the profiles from the surface to 500 hPa was assimilated (not shown). The results from this sensitivity test were consistent with those of the full-profile assimilation, reinforcing the robustness of the original findings.

4. Experiment Results

4.1. Verifying the Effects of Assimilating Pseudo Wind Profiles

To assess the impact of wind profile assimilation, we first compared the wind profile differences between "Bad" member and "Good" member experiments, as well as between different DA experiments and "Good" member at the corresponding assimilated locations. For DA_All, the wind profile differences were averaged across the three selected locations (Figure 5).

The results indicate that, prior to assimilation, substantial discrepancies existed between "Bad" member and "Good" member at three locations (Figures 5a1, 5b1, and 5c1). In particular, at the assimilated locations used in DA_Nor and DA_SW, meridional wind differences around 950 hPa exceeded 4 m s^{-1} (Figures 5a1 and 5b1), indicating large errors in the representation of the marine BLJ. After applying 3DVAR, these discrepancies were significantly reduced, demonstrating the effectiveness of wind profile assimilation. Specifically, the underestimated southerly winds in "Bad" member were effectively corrected in the DA experiments (Figures 5a2, 5b2, and 5d2). In DA_SE, the primary improvement was the correction of the overestimated westerly wind in "Bad" member (Figure 5c2). These results suggest that different DA experiments led to location-specific improvements, refining the representation of the marine BLJ and its associated wind structure.

To further evaluate the impact of these wind profile adjustments, we next examined their influences on rainfall simulations. Figure 6 presents the simulated radar reflectivity between 19:00 and 21:00 UTC across different experiments. According to the definition by Weckwerth and Parsons (2006), convection initiation (CI) is

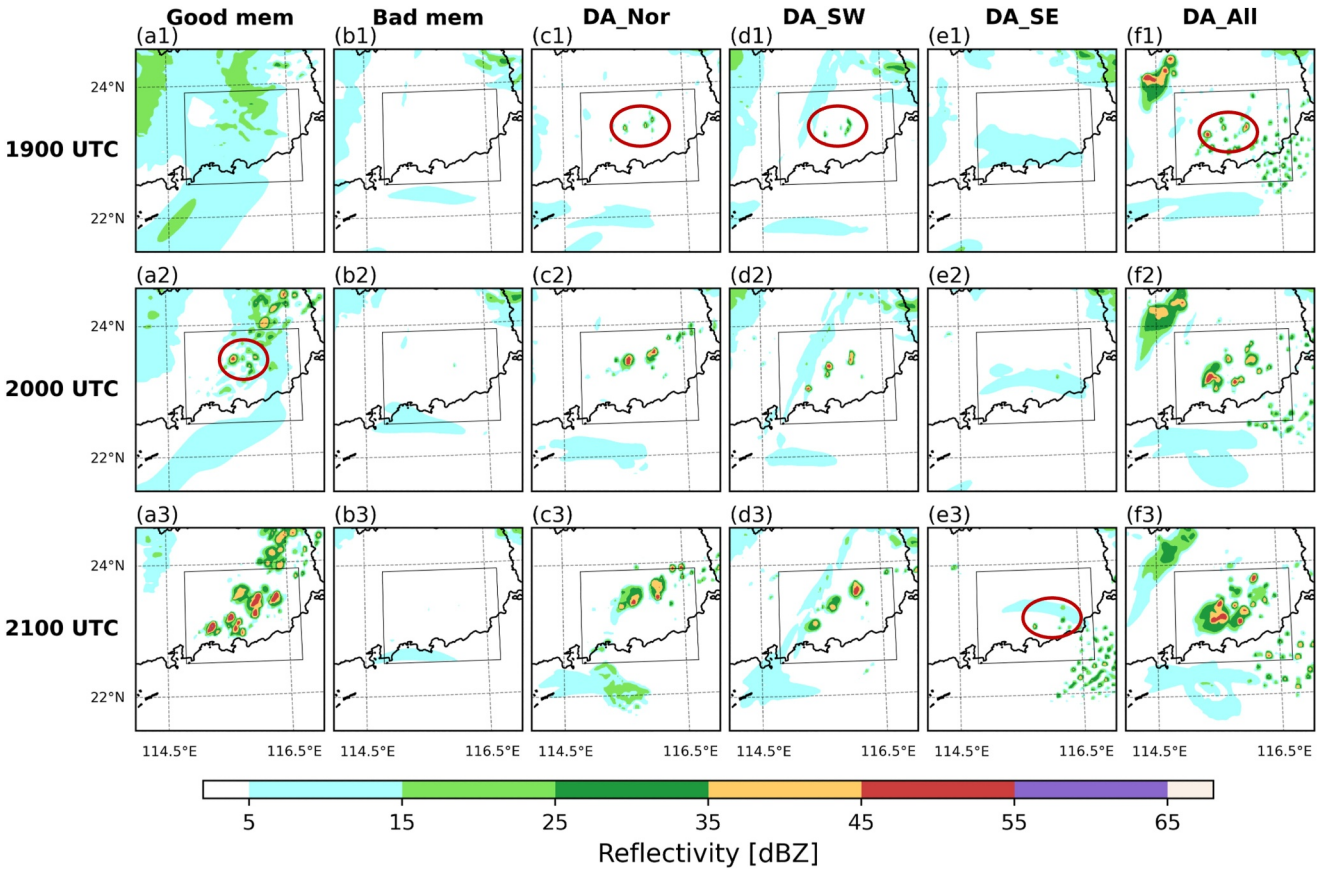

Figure 6. Simulated hourly radar composite reflectivity (shaded) from 19:00 UTC to 21:00 UTC on 21 June 2018 for (a1–a3) "Good" member, (b1–b3) "Bad" member, (c1–c3) DA_Nor, (d1–d3) DA_SW, (e1–e3) DA_SE, and (f1–f3) DA_All. Red ellipses indicate the locations of convection initiation.

identified when radar reflectivity exceeds 35 dBZ for the first time. At 20:00 UTC, significant CI was observed in "Good" member (Figure 6a2), whereas "Bad" member failed to produce any CI (Figures 6b1-6b3).

All four DA experiments (DA_Nor, DA_SW, DA_SE, and DA_All) successfully captured CI, though with variations in timing and intensity. DA_Nor, DA_SW, and DA_All initiated convection at 19:00 UTC, two hours earlier than DA_SE (Figures 6c–6f). Notably, both DA_Nor and DA_All produced stronger convective activity than "Good" member at 2000 UTC (Figures 6a2, 6c2, and 6f2). In terms of convective structure, DA_Nor and DA_SW generated few dominant convective cell (Figures 6c2 and 6d2) while DA_All produced multiple smaller convective cells (Figure 6f2).

Figure 7 compares the 6-hr accumulated precipitation from 18:00 UTC 21 June to 00:00 UTC 22 June across the different experiments (Figures 7a–7f). All DA experiments showed improved rainfall simulations compared to "Bad" member. Among them, DA_All exhibited the most extensive convection zone, whereas DA_Nor produced the most intense and concentrated convection. In contrast, DA_SW yielded only minor improvement over "Bad" member and only negligible improvement was observed in DA_SE.

We further analyzed the temporal evolution of hourly maximum rainfall. Before 20:00 UTC, all DA experiments outperformed "Bad" member, which produced no precipitation throughout the period. However, after 20:00 UTC, "Good" member significantly outperformed all other experiments. While convection intensity in the DA experiments either plateaued or weakened, "Good" member continued to intensify, eventually exceeding 100 mm hr^{-1}.

The dynamic and thermodynamic effects of the marine BLJ on CI and UCG have been extensively documented by Du, Chen, Han, Mai, et al. (2020) and Du, Chen, Han, Bai, and Li (2020). Building upon their findings, the following section investigates whether the DA process enhances the intensity and structure of the marine BLJ, and consequently contributes to improved simulations of coastal warm-sector heavy rainfall.

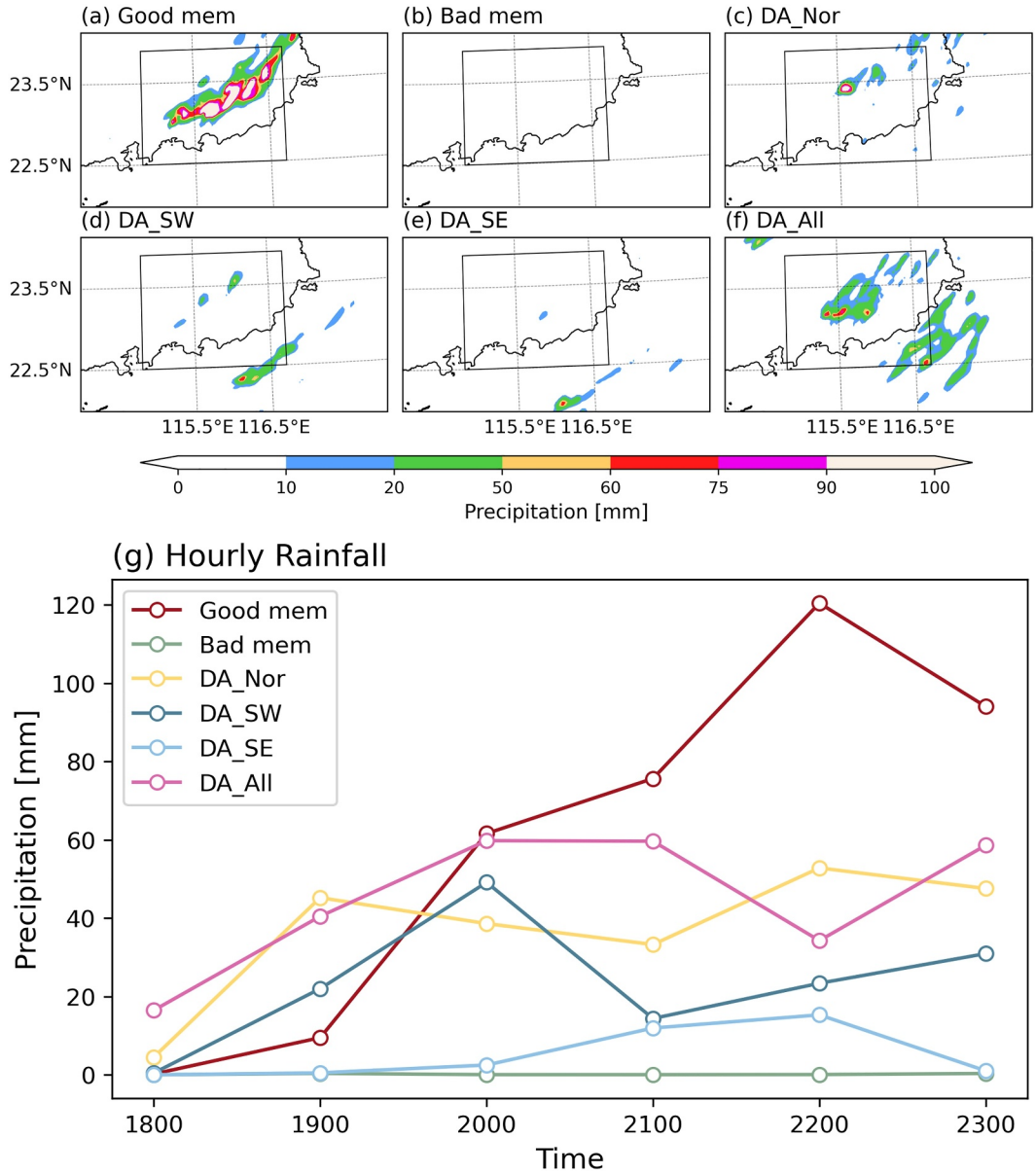

Figure 7. The distribution of 6-hr accumulated precipitation from 18:00 UTC 21 June to 00:00 UTC 22 June for (a) "Good" member, (b) "Bad" member, (c) DA_Nor, (d) DA_SW, (e) DA_SE, and (f) DA_All. (g) Hourly maximum rainfall in the core region (black box in Figure 1b).

4.2. Performance of the Boundary Layer Jet Over the Northern South China Sea

Figure 8 presents the evolution of the 950-hPa horizontal wind field from 12:00 UTC to 18:00 UTC across different experiments. At the initial analysis time (12:00 UTC), the structure and intensity of the BLJs varied significantly among the experiments. As discussed previously, "Good" member featured a stronger southerly wind component, with wind speed exceeding 8 m s^{-1}, extending farther northward, and the upstream core located farther west, near 112°E. In contrast, "Bad" member exhibited a more pronounced westerly wind component, with the jet extending farther south and its upstream core was located farther east, around 116°E (Figures 8a1 and 8b1).

Following the application of the 3DVAR data assimilation, all DA experiments exhibited varying degrees of BLJ intensification (Figures 8c1–8f1). DA_Nor showed significant strengthening of the BLJ, accompanied by a pronounced shift toward a more southerly wind direction compared with "Bad" member. Wind speed exceeded

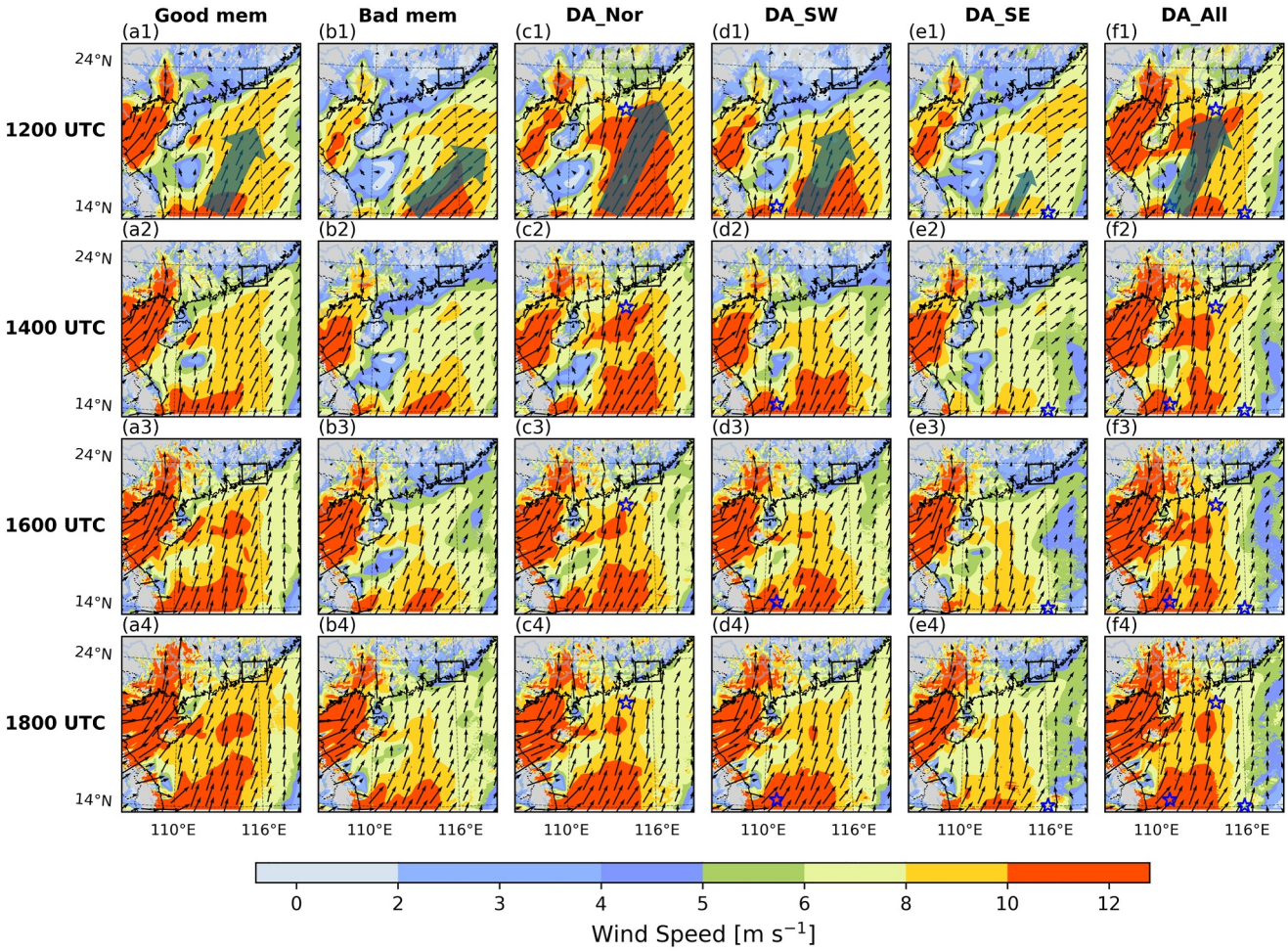

Figure 8. Horizontal distribution of wind speed (shaded) and vectors at 950 hPa for (a1–a4) "Good" member, (b1–b4) "Bad" member, (c1–c4) DA_Nor, (d1–d4) DA_SW, (e1–e4) DA_SE, and (f1–f4) DA_All from 12:00 UTC to 18:00 UTC 21 June 2018. The black boxes are the same as in Figure 1b. The blue stars correspond to those in Figure 4. Transparent arrows represent the general direction and relative intensity of the boundary layer jet for comparison among experiments.

10 m s^{-1} across a large portion of the region, indicating a marked increase in intensity. DA_SW mainly enhanced the upstream portion of the BLJ, reducing the westerly component, resulting in a more dominant southerly wind and a farther west upstream jet core. DA_SE produced the weakest BLJ among the DA experiments. This stemmed from a substantial weakening of the westerly wind component, although a strong southwesterly flow persisted to the southeast of South China, closely resembling "Bad" member. In DA_All, the horizontal wind field closely mirrored "Good" member with only minor differences that there was slightly stronger winds over the ocean south of Guangdong Province, suggesting that assimilating wind profiles from multiple locations yielded the most accurate reconstruction of the BLJ.

It is noteworthy that the DA_Nor experiment, which assimilated only a single wind profile near the coast, exhibited a stronger BLJ at the initial time compared with the DA_All experiment, which assimilated three profiles. This outcome is attributed to the limited spatial constraint in DA_Nor. With only one observational input, the assimilation system lacks sufficient information to balance wind field adjustments regionally, which may result in a localized over-amplification of the jet. In contrast, the broader observational coverage in DA_All allows for more spatially distributed increments and yields a more balanced and realistic initial wind structure.

As the simulation progressed, most experiments showed a gradual northward extension of the BLJ. Notably, DA_Nor had already established a strong and well-developed BLJ across the entire NSCS from the beginning. By 1800 UTC, shortly before CI, the BLJ in "Good" member had nearly reached the south coast of China, serving as a crucial precursor to rainfall development. Among the DA experiments, DA_All exhibited the most similar

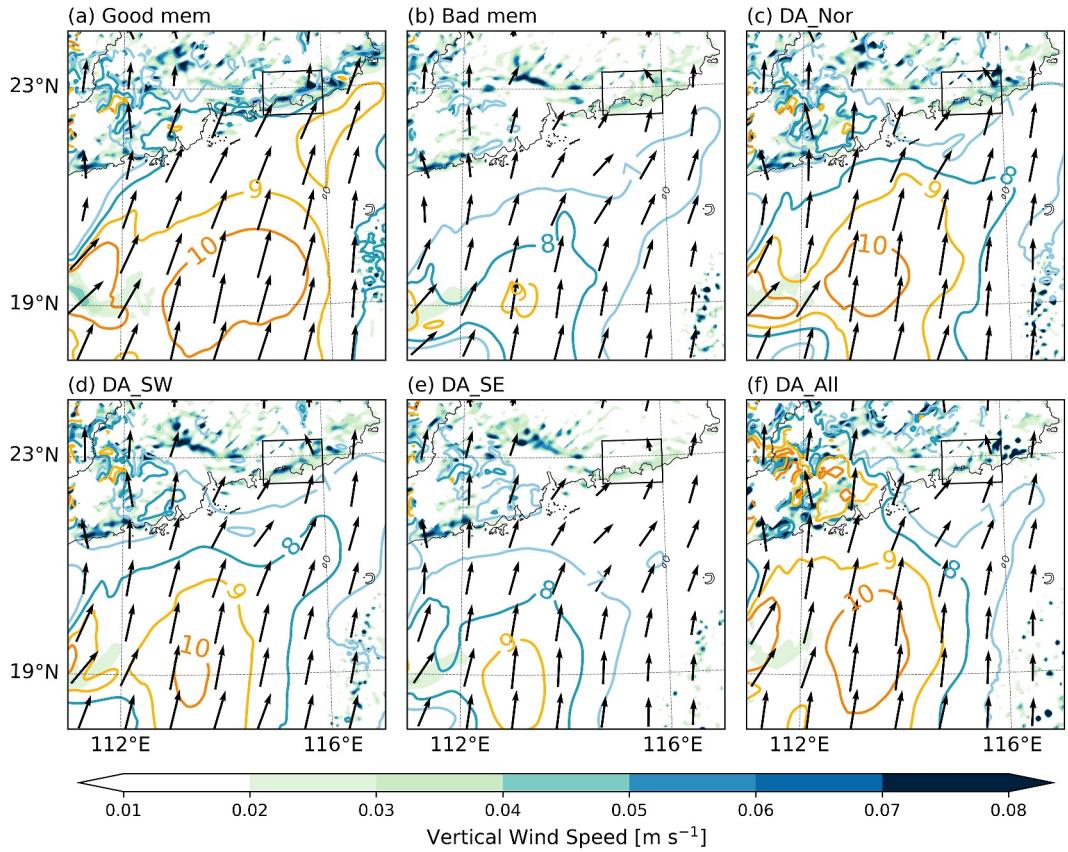

Figure 9. Vertical motion (shaded) at 950 hPa, horizontal wind speeds (contours = 7, 8, 9, and 10 m s^{-1}), and wind vectors at 950 hPa for (a) "Good" member, (b) "Bad" member, (c) DA_Nor, (d) DA_SW, (e) DA_SE, and (f) DA_All at 18:00 UTC 21 June. The black boxes are the same as in Figure 1b.

evolution to "Good" member, though it remained slightly weaker over the ocean south of Guangdong Province. DA_Nor, which initially featured the strongest BLJ, experienced a gradual slight weakening, eventually resembling DA_SW in intensity and structure. In contrast, DA_SW underwent progressive strengthening of the BLJ over time, gradually narrowing the gap with "Good" member in both intensity and structure. Meanwhile, DA_SE consistently remained the weakest throughout the period, maintaining a BLJ strength comparable to "Bad" member, but with a reduced westerly component. These differences underscore the spatial sensitivity of wind profile assimilation, emphasizing how the locations of observations critically influences the evolution and intensity of the marine BLJ.

4.2.1. Dynamic Effect of the Boundary Layer Jet

Building on the findings of Du, Chen, Han, Bai, and Li (2020), which confirmed the dynamic and thermodynamic effects of BLJs on warm-sector heavy rainfall, we first analyzed their dynamic impact—specifically, the strong ascending motion induced by low-level convergence at the BLJ terminus.

As shown in Figure 9, the low-level vertical motion along the South China coast varied across different experiments. DA_Nor, DA_SW, and DA_All exhibited notable improvements in coastal ascent compared with "Bad" member, primarily due to the intensified BLJ, which led to increased wind speeds both upstream and near the coast (Figures 9c, 9d, and 9f). This enhancement amplified low-level convergence, thereby reinforcing vertical motion. In contrast, DA_SE exhibited only marginal improvement in vertical motion. Although its upstream BLJ slightly strengthened, the wind intensity near the coast remained nearly unchanged compared to "Bad" member. As a result, vertical motion in DA_SE remained weaker than in the other DA experiments (Figure 9e), highlighting the limited dynamic impact of assimilating wind profile only at the southeastern core.

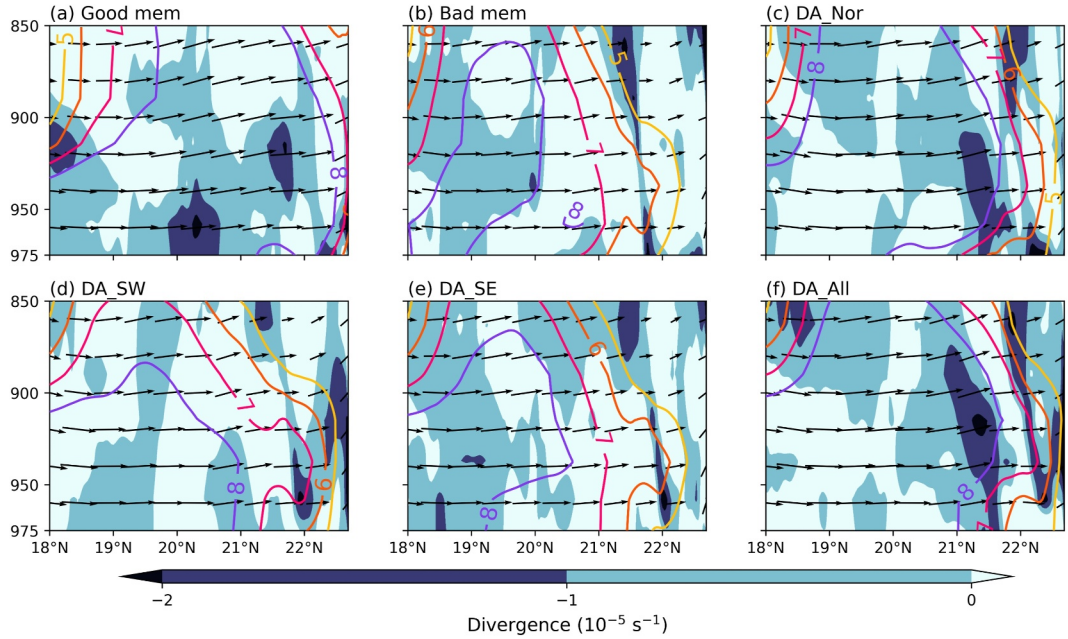

Figure 10. Vertical cross sections of divergence (shaded, calculated as the deviation from the six-experiment mean), wind speed (contours, m s^{-1}), and flow vectors (black vectors along the cross-section with vertical velocity amplified by 100) along the blue line in Figure 4 at 18:00 UTC 21 June from (a) "Good" member, (b) "Bad" member, (c) DA_Nor, (d) DA_SW, (e) DA_SE, and (f) DA_All. Note that the contour lines represent the horizontal wind speed projected along the cross section.

To better illustrate the improvements in low-level vertical motion along the South China coast, a cross-section analysis was performed along the blue line in Figure 4a to assess convergence at the terminus of the BLJ. The results show that in "Bad" member, convergence was significantly shallower than in "Good" member (Figures 10a and 10b). Similarly, in DA_Nor, DA_SW, and DA_All, stronger convergence occurred near the coast due to a more pronounced horizontal wind speed gradient (Figures 10c, 10d, and 10f), leading to enhanced vertical motion. Conversely, DA_SE displayed a convergence structure comparable in both intensity and vertical extent to that of "Bad" member (Figure 10e), consistent with its weaker associated vertical motion.

In summary, the above analysis demonstrates that assimilating wind information near the core and terminal regions of the BLJ can help achieve a better representation of key dynamical fields (DA_Nor, DA_SW, and DA_All). Although the southeastern core exhibits a large difference in BLJ structure between "Good" member and "Bad" member, this difference mainly results from a stronger westerly component in "Bad" member, whereas "Good" member shows a stronger southerly component. Therefore, when assimilating wind profile at the southeastern core, the analysis tends to reduce the u-component in that region, which fails to effectively improve the representation of the BLJ core and terminal structure as seen in "Good" member, and consequently leads to limited improvement in the forecast of warm-sector heavy rainfall. In addition to dynamic effects, the next section examines the thermodynamic effects associated with BLJs across different experiments to further explore their influences on CI.

4.2.2. Thermodynamic Effect of the Boundary Layer Jet

The thermodynamic effect of the BLJ plays a crucial role in transporting large amounts of warm, moist air, thereby creating a humid and unstable environment conducive to deep convection. Figure 11a illustrates the evolution of the area-averaged water vapor mixing ratio (q_v) over the core convection region across different experiments. Between 12:00 and 18:00 UTC on 21 June 2018, q_v increases in all experiments from approximately 17.6 g kg^{-1} to over 18 g kg^{-1}. As expected, "Bad" member and DA_SE exhibited the lowest q_v after 14:00 UTC, resulting in relatively drier environments before CI. By 18:00 UTC, q_v in DA_Nor, DA_SW, and DA_All exceeded that in "Bad" member by approximately 0.2–0.5 g kg^{-1}, indicating a moister environment more favorable for CI.

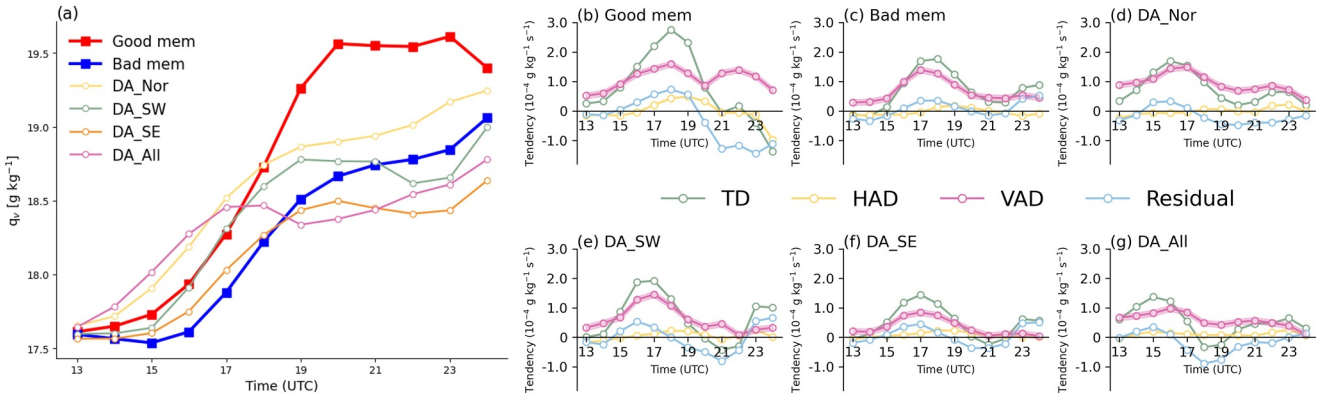

Figure 11. (a) Evolutions of water vapor mixing ratio (q_v, g kg^{-1}) averaged over the core convection area (as denoted in Figure 1b). (b–g) Evolutions of area-averaged local tendency (green line) of q_v (g kg^{-1} s^{-1}) at 950 hPa, along with its components including horizontal transport (yellow line), vertical transport (purple line), and residual term (blue line) for (b) "Good" member, (c) "Bad" member, (d) DA_Nor, (e) DA_SW, (f) DA_SE, and (g) DA_All.

In order to better evaluate the impact of wind profile assimilation on moisture transport, we calculated the vertically integrated moisture flux convergence (VIMFC) from 1,000 hPa to 850 hPa over the coastal region, averaged before 18:00 UTC. Results show a noticeable enhancement in all DA experiments compared to "Bad" member, with increase of 28.97% (DA_Nor), 80.18% (DA_SW), and 66.70% (DA_All). These findings underscore the importance of strengthened low-level moisture convergence in facilitating convective development and enhancing rainfall.

To further investigate the processes driving the increase in q_v at 950 hPa, a quantitative diagnosis of the q_v budget was performed (Figures 11b–11g), with all terms in Equation 3 averaged over the core convection region. The results indicate that vertical transport was the primary driver of local moistening across all experiments. Moisture was primarily transported upward from lower levels with higher water vapor content, associated with mesoscale ascent near the BLJ terminus, whereas horizontal transport played a secondary role.

In "Good" member, DA_Nor, DA_SW, and DA_All, the vertical transport term started increasing after 13:00 UTC, whereas in "Bad" member, a notable increase was not observed until after 15:00 UTC. This temporal lag resulted in a cumulative moisture deficit in "Bad" member before CI, contributing to the observed drier conditions. Notably, DA_SE showed a slight decrease relative to "Bad" member, which was consistent with its limited rainfall and weak BLJ, resembling the behavior of "Bad" member.

Note that the residual term in "Good" member became substantially negative after 21:00 UTC. As described in Section 2.4, this residual term includes contributions from condensation-related processes. Among all experiments, "Good" member exhibited the most intense convective activity, implying a large amount of water vapor consumed through condensation, which contributed to the strongly negative residual values.

4.3. Upscale Convective Growth in Different Experiments

After assimilating wind profiles, the stronger BLJ enhanced both lifting and moisture transport, thereby creating more favorable conditions for CI. However, as shown in Figures 6a3–6f3 and 7a, significant discrepancies remained between the DA experiments and "Good" member in both the intensity and spatial coverage of the convection and precipitation. We also found that the convective available potential energy (CAPE) in the coastal region of "Good" member exceeded 1,800 J kg^{-1}—substantially higher than the values in other experiments, where CAPE ranged from approximately 1,000 to 1,400 J kg^{-1} (not shown). To explore the underlying causes of these differences, we further investigated the evolution of the 950-hPa horizontal wind field after 18:00 UTC (Figure 12).

A strong correlation was evident between convection (deep blue shading) and low-level divergence (pink contours). In "Good" member, the UCG process began after 20:00 UTC, with convection becoming stronger and more organized as the BLJ strengthens and exceeds 10 m s^{-1} near the coast (Figures 12a3 and 12a4). In contrast, DA_All, despite featuring the strongest BLJ among the DA experiments, only exhibited merging and

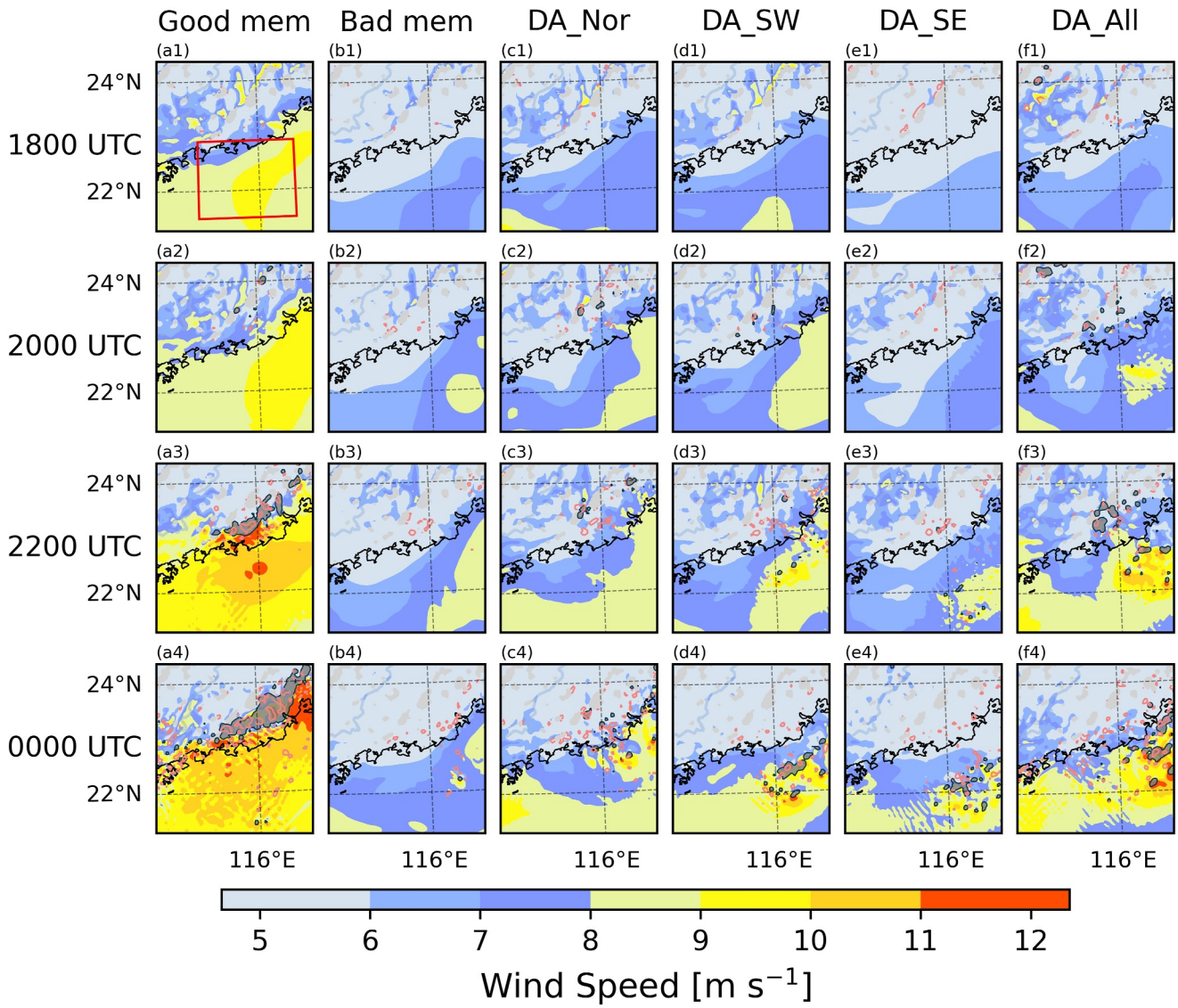

Figure 12. Horizontal distribution of wind speed (shaded) at 950 hPa from 18:00 UTC 21 June to 00:00 UTC 22 June 2018 for (a1–a4) "Good" member, (b1–b4) "Bad" member, (c1–c4) DA_Nor, (d1–d4) DA_SW, (e1–e4) DA_SE, and (f1–f4) DA_All. Deep blue shading represents reflectivity greater than 35 dBZ, and pink contours represent divergence exceeding 2 × 10^{-5} s^{-1}.

intensification of small-scale convective cells, with full organization not occurring until 22:00 UTC. Two hours later, convection over land dissipated (Figures 12f2–12f4). Other DA experiments and "Bad" member exhibited even fewer or no convective cells, likely due to their weaker coastal BLJ. In "Good" member, the BLJ extended beyond the coastline, promoting enhanced moisture transport and facilitating the UCG process.

The differences in moisture transport were further reflected in the evolution of q_v. After 19:00 UTC, q_v in "Good" member continued increasing for another hour, stabilizing at a high level of 19.5 g kg^{-1}. In contrast, other experiments maintained lower q_v values under 19 g kg^{-1}, suggesting a less favorable environment for UCG. Notably, all DA experiments developed moderate convection over the ocean, where the BLJ terminated and generated favorable ascent motions (Figures 12c4, 12d4, 12e4, and 12f4).

To understand why the BLJs in "Bad" member and DA experiments failed to extend northward and intensify as in "Good" member, we analyzed the evolutions of the meridional wind component and conducted a quantitative momentum budget diagnosis (Figure 13). The results show that only in "Good" member did the meridional wind

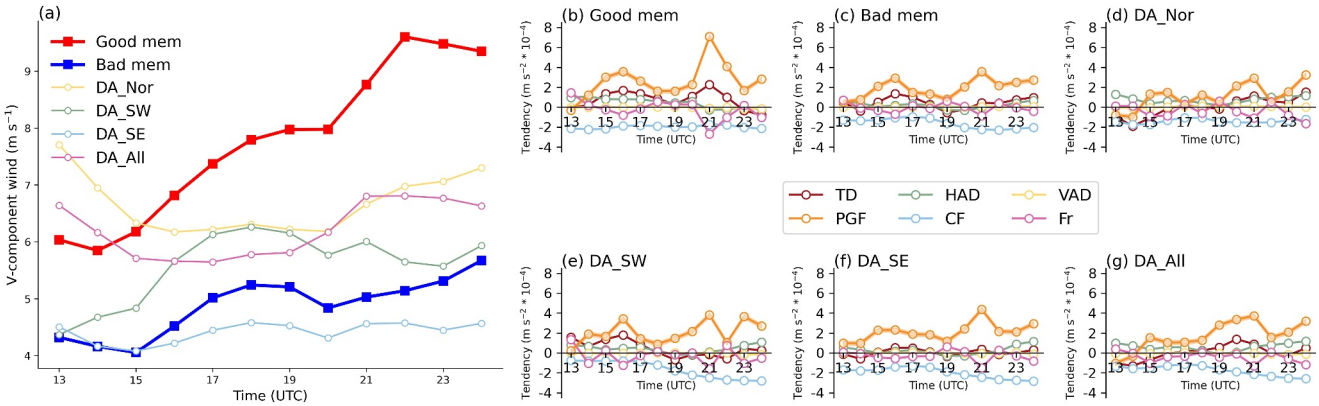

Figure 13. (a) Evolutions of meridional wind at 950 hPa (m s^{-1}) averaged over the area indicated in Figure 12a1. (b–g) Evolutions of area-averaged local wind tendency (red line, m s^{-2}), along with its contributing components including horizontal transport (green line), vertical transport (yellow line), pressure gradient force (orange line), Coriolis force (blue line), and friction force (purple line) for (b) "Good" member, (c) "Bad" member, (d) DA_Nor, (e) DA_SW, (f) DA_SE, and (g) DA_All.

continue to strengthen after 20:00 UTC, exceeding 9 m s^{-1}. In contrast, all other experiments remained below 8 m s^{-1} (Figure 13a).

Further examination of the momentum budget reveals that the PGF played a key role in modulating wind acceleration. In "Good" member, the PGF term was significantly larger than in other experiments, resulting in strong positive wind tendency after 2000 UTC (Figure 13b). In contrast, the weaker initial wind speed and PGF in "Bad" member prevented the BLJ from intensifying near the coast (Figure 13c).

Among the DA experiments, DA_Nor initially experienced rapid intensification of the meridional wind near the coast due to 3DVAR assimilation. However, an imbalance between the wind and pressure fields caused the PGF term to turn negative, leading to a sharp decrease in wind speed. Despite this, DA_Nor maintained wind speeds approximately 2 m s^{-1} higher than "Bad" member, sufficient for CI but insufficient to sustain UCG (Figure 13a). In DA_SW, where the upstream BLJ was assimilated, both the PGF and horizontal advection (HAD) terms increased, strengthening the meridional wind near the coast. However, this strengthening ceased abruptly after 18:00 UTC, limiting further intensification (Figure 13e). DA_SE showed minimal differences from "Bad" member, consistent with the findings in Section 4.1 (Figure 13f). DA_All initially behaved similarly to DA_Nor, with strong coastal wind speeds that subsequently weakened by the PGF term. After 18:00 UTC, a slight intensification occurred, but it remained weaker than in "Good" member, leading to late convection over the ocean rather than over land (Figure 13g).

5. Conclusions and Discussions

This study conducted an OSSE to investigate the impact of assimilating wind profile observations near the BLJ over the South China Sea on the simulations of coastal warm-sector heavy rainfall. Using 3DVAR data assimilation, four experiments were designed—DA_Nor, DA_SW, and DA_SE—each assimilating wind profiles from specific location, with DA_All incorporating all three.

Compared with "Bad" member experiment, which failed to initiate convection or produce precipitation, only DA_Nor, DA_SW, and DA_All experiments exhibited marked improvement in 6-hr accumulated precipitation. These improvements were primarily due to enhanced representations of the marine BLJ. In DA_Nor, DA_SW, and DA_All experiments, both dynamic and thermodynamic effects associated with the marine BLJ contribute to convective initiation. In contrast, the DA_SE experiment showed only limited improvement, likely due to the relatively weak impact of assimilating wind profiles from the southeastern core region. Nonetheless, none of the DA experiments successfully replicated the rainfall intensity of "Good" member, largely due to their failure to reproduce the UCG process.

The wind profile assimilation dynamically improved the low-level wind field and intensified the marine BLJ near the coastal region. As the BLJ extended northward, its terminus reached the coastal region, generating ascending motion and creating a favorable dynamic environment for convection initiation (CI). In DA_Nor, the BLJ nearly

maintained its strength near the coast, continuously supporting strong upward motion for convection development. In DA_SW, the BLJ gradually extended toward the coast, enhancing ascent. DA_All, like the DA_Nor but with more assimilated profiles, closely resembled "Good" member. In contrast, DA_SE showed minimal improvement in the wind field compared to "Bad" member, resulting in limited dynamic support for convection.

Our findings also highlight the crucial role of BLJ-induced thermodynamic effects in regulating moisture content and convective instability. Wind profile assimilation increased water vapor mixing ratios in the core convection region, creating a more humid and unstable environment favorable for CI. A water vapor budget analysis revealed that vertical transport was the primary contributor to local moistening across the DA experiments, with earlier and stronger upward transport compared to "Bad" member. In DA_SE, however, showed only a slight increase in moisture relative to "Bad" member, consistent with its limited rainfall and weak BLJ, closely resembling the behavior of "Bad" member. These results underscore the importance of assimilating wind profiles to better represent BLJ dynamics and thermodynamics for improved simulation of coastal warm-sector heavy rainfall.

Despite the improvements in CI, significant discrepancies in precipitation intensity and spatial distribution remained between the DA experiments and "Good" member. The main limiting factor was the failure of the BLJ in the DA experiments to extend further north and intensify, restricting UCG. Momentum budget analysis indicated that "Good" member featured a stronger PGF, which sustained meridional wind acceleration and BLJ intensification after 20:00 UTC. In contrast, the DA experiments, particularly DA_Nor and DA_SW, showed initial enhancements in coastal meridional wind, but these then weakened due to a reduction in PGF, thereby limiting BLJ strengthening and suppressing UCG. DA_SE showed the weakest response, highlighting the spatial sensitivity of wind assimilation impacts.

In summary, this OSSE study demonstrates that assimilating wind profiles near the marine BLJ significantly improves the representation of CI, though its influence on subsequent convective organization and upscale growth remains limited. The impact of assimilation is strongly location-dependent, underscoring the importance of strategically placed observations. These findings offer valuable insights for optimizing observational strategies in future field campaigns. Specifically, wind profile data from both the core and terminal regions of the BLJ are crucial: while the core region adjusts the dynamical structure of the jet, and the terminal region more directly affects the forecast accuracy of warm-sector heavy rainfall in South China. Therefore, future observational designs should prioritize coverage of both regions to improve forecasting performance.

This study also has several limitations that suggest avenues for future research. For instance, multiple assimilation cycles were not performed in this study due to the low temporal resolution of radiosonde observations. In future work, high-temporal-resolution data, such as radar wind profiler (RWP) observations, will be explored to enable multi-cycle assimilation, aiming to better capture the evolution of coastal dynamics and convection. Additionally, further investigations involving multiple cases are necessary to assess the robustness and event-to-event variability of the impacts of wind profile assimilation on the predictability of warm-sector heavy rainfall.

Data Availability Statement

The CMORPH data can be accessed at https://www.ncei.noaa.gov/products/climate-data-records/precipitation-cmorph (Xie et al., 2019). The ERA5 reanalysis data were from ECMWF via https://cds.climate.copernicus.eu/datasets/reanalysis-era5-pressure-levels?tab=overview (Hersbach et al., 2018). NOAA Global Ensemble Forecast System (GEFS) was accessed from https://registry.opendata.aws/noaa-gefs. Version 4.5.1 of the WRF model used for numerical simulation in this study can be accessed at https://www2.mmm.ucar.edu/wrf/users/download/get_source.html (Skamarock et al., 2019). Version 4.5.1 of the WRFDA used for data assimilation in this study can be accessed at https://www2.mmm.ucar.edu/wrf/users/wrfda/downloads.html (Barker et al., 2004a).

Acknowledgments
This study was supported by project supported by Southern Marine Science and Engineering Guangdong Laboratory (Zhuhai) (SML2024SP035, SML2024SP012, and 311024001), the Guangdong Project of Basic and Applied Basic Research (Grant 2024A1515510005 and 2025A1515011974), the National Natural Science Foundation of China (Grants 42475002), and the Key Innovation Team of the China Meteorological Administration (CMA2023ZD08). We also acknowledge the high-performance computing support from School of Atmospheric Sciences of Sun Yat-sen University.

References

Bai, L., Chen, G., Huang, Y., & Meng, Z. (2021). Convection initiation at a coastal rainfall hotspot in south China: Synoptic patterns and orographic effects. *Journal of Geophysical Research: Atmospheres*, *126*(24), e2021JD034642. https://doi.org/10.1029/2021JD034642

Barker, D., Huang, W., Guo, Y.-R., & Bourgeois, A. (2003). A three-dimensional variational (3DVAR) data assimilation system for use with MM5. *NCAR Tech Note*, *68*.

Barker, D., Huang, W., Guo, Y.-R., Bourgeois, A., & Xiao, Q. (2004a). A three-dimensional variational data assimilation system for MM5: Implementation and initial results [software]. *Monthly Weather Review*, *132*(4), 897–914. https://doi.org/10.1175/1520-0493(2004)132<0897:atvdas>2.0.co;2

Barker, D. M., Huang, W., Guo, Y.-R., Bourgeois, A. J., & Xiao, Q. N. (2004b). A three-dimensional variational data assimilation system for MM5: Implementation and initial results. Retrieved from https://journals.ametsoc.org/view/journals/mwre/132/4/1520-0493_2004_132_0897_atvdas_2.0.co_2.xml

Chen, G., Sha, W., Iwasaki, T., & Wen, Z. (2017). Diurnal cycle of a heavy rainfall corridor over East Asia. *Monthly Weather Review*, *145*(8), 3365–3389. https://doi.org/10.1175/MWR-D-16-0423.1

Chen, S.-H., Chen, J.-Y., Chang, W.-Y., Lin, P.-L., Lin, P.-H., & Sun, W.-Y. (2011). Observing system simulation experiment: Development of the system and preliminary results. *Journal of Geophysical Research*, *116*(D13), D13202. https://doi.org/10.1029/2010JD015103

Chen, X., Zhang, F., & Zhao, K. (2016). Diurnal variations of the land–sea breeze and its related precipitation over south China. https://doi.org/10.1175/JAS-D-16-0106.1

Courtier, P., Thépaut, J.-N., & Hollingsworth, A. (1994). A strategy for operational implementation of 4D-Var, using an incremental approach. *Quarterly Journal of the Royal Meteorological Society*, *120*(519), 1367–1387. https://doi.org/10.1002/qj.49712051912

Ding, Y. (1994). *Monsoons over China*. Kluwer Academic Publishers.

Dong, F., Zhi, X., Zhang, L., & Ye, C. (2021). Diurnal variations of coastal boundary layer jets over the northern South China Sea and their impacts on diurnal cycle of rainfall over southern China during the early-summer rainy season. https://doi.org/10.1175/MWR-D-20-0292.1

Du, Y., & Chen, G. (2018). Heavy rainfall associated with double low-level jets over southern China. *Part I: Ensemble-Based Analysis*, *146*(11), 3827–3844. https://doi.org/10.1175/MWR-D-18-0101.1

Du, Y., & Chen, G. (2019). Heavy rainfall associated with double low-level jets over southern China. Part II: Convection initiation. https://doi.org/10.1175/MWR-D-18-0102.1

Du, Y., Chen, G., Han, B., Bai, L., & Li, M. (2020). Convection initiation and growth at the Coast of south China. *Part II: Effects of the Terrain, Coastline, and Cold Pools*, *148*(9), 3871–3892. https://doi.org/10.1175/MWR-D-20-0090.1

Du, Y., Chen, G., Han, B., Mai, C., Bai, L., & Li, M. (2020). Convection initiation and growth at the coast of South China. Part I: Effect of the marine boundary layer jet. *Monthly Weather Review*, *148*(9), 3847–3869. https://doi.org/10.1175/MWR-D-20-0089.1

Du, Y., Rotunno, R., & Zhang, Q. (2015). Analysis of WRF-simulated diurnal boundary layer winds in eastern China using a simple 1D model. *Journal of the Atmospheric Sciences*, *72*(2), 714–727. https://doi.org/10.1175/jas-d-14-0186.1

Du, Y., Shen, Y., & Chen, G. (2022). Influence of coastal marine boundary layer jets on rainfall in South China. *Advances in Atmospheric Sciences*, *39*(5), 782–801. https://doi.org/10.1007/s00376-021-1195-7

Du, Y., Zhang, Q., Chen, Y., Zhao, Y., & Wang, X. (2014). Numerical simulations of spatial distributions and diurnal variations of low-level jets in China during early summer. *Journal of Climate*, *27*(15), 5747–5767. https://doi.org/10.1175/jcli-d-13-00571.1

Gao, X., Luo, Y., Lin, Y., & Bao, X. (2022). A source of WRF simulation error for the early-summer warm-sector heavy rainfall over south China Coast: Land-sea thermal contrast in the boundary layer. *Journal of Geophysical Research: Atmospheres*, *127*(4), e2021JD035179. https://doi.org/10.1029/2021JD035179

Ha, J. H., Kim, H. W., & Lee, D. K. (2011). Observation and numerical simulations with radar and surface data assimilation for heavy rainfall over central Korea. *Advances in Atmospheric Sciences*, *28*(3), 573–590. https://doi.org/10.1007/s00376-010-0035-y

Hersbach, H., Bell, B., Berrisford, P., Biavati, G., Horányi, A., Muñoz Sabater, J., et al. (2018). ERA5 hourly data on pressure levels from 1979 to present [Dataset]. *Copernicus Climate Change Service (C3s) Climate Data Store (Cds)*, *10*(10.24381). https://doi.org/10.24381/cds.bd0915c6

Hong, S.-Y., Noh, Y., & Dudhia, J. (2006). A new vertical diffusion package with an explicit treatment of entrainment processes. *Monthly Weather Review*, *134*(9), 2318–2341. https://doi.org/10.1175/mwr3199.1

Hou, T., Kong, F., Chen, X., Lei, H., & Hu, Z. (2015). Evaluation of radar and automatic weather station data assimilation for a heavy rainfall event in southern China. *Advances in Atmospheric Sciences*, *32*(7), 967–978. https://doi.org/10.1007/s00376-014-4155-7

Hu, H., Sun, J., & Zhang, Q. (2017). Assessing the impact of surface and wind profiler data on fog forecasting using WRF 3DVAR: An OSSE study on a dense fog event over north China. https://doi.org/10.1175/JAMC-D-16-0246.1

Huang, S., Li, Z., Bao, C., Yu, Z., Chen, H., Yu, S., et al. (1986). *Heavy rainfall over southern China in the pre-summer rainy season* (Vol. 244). Guangdong Science and Technology Press.

Huang, X.-Y., Gao, F., Jacobs, N. A., & and, H. W. (2013). Assimilation of wind speed and direction observations: A new formulation and results from idealised experiments. *Tellus A: Dynamic Meteorology and Oceanography*, *65*(1), 19936. https://doi.org/10.3402/tellusa.v65i0.19936

Huo, Z., Liu, Y., Shi, Y., Chen, B., Fan, H., & Li, Y. (2023). An investigation on joint data assimilation of a radar network and ground-based profiling platforms for forecasting convective storms. https://doi.org/10.1175/MWR-D-22-0332.1

Iacono, M. J., Delamere, J. S., Mlawer, E. J., Shephard, M. W., Clough, S. A., & Collins, W. D. (2008). Radiative forcing by long-lived greenhouse gases: Calculations with the AER radiative transfer models. *Journal of Geophysical Research*, *113*(D13). https://doi.org/10.1029/2008jd009944

Jiménez, P. A., Dudhia, J., González-Rouco, J. F., Navarro, J., Montávez, J. P., & García-Bustamante, E. (2012). A revised scheme for the WRF surface layer formulation. *Monthly Weather Review*, *140*(3), 898–918. https://doi.org/10.1175/mwr-d-11-00056.1

Kain, J. S. (2004). The Kain–Fritsch convective parameterization: An update. *Journal of Applied Meteorology*, *43*(1), 170–181. https://doi.org/10.1175/1520-0450(2004)043<0170:tkcpau>2.0.co;2

Li, X., & Du, Y. (2021). Statistical relationships between two types of heavy rainfall and low-level jets in south China. https://doi.org/10.1175/JCLI-D-21-0121.1

Li, Z., Luo, Y., Du, Y., & Chan, J. C. L. (2020). Statistical characteristics of pre-summer rainfall over south China and associated synoptic conditions. *Journal of the Meteorological Society of Japan. Ser. II*, *98*(1), 213–233. https://doi.org/10.2151/jmsj.2020-012

Livneh, B., Restrepo, P. J., & Lettenmaier, D. P. (2011). Development of a unified land model for prediction of surface hydrology and land–atmosphere interactions. *Journal of Hydrometeorology*, *12*(6), 1299–1320. https://doi.org/10.1175/2011jhm1361.1

Luo, Y., & Du, Y. (2023). The roles of low-level jets in "21·7" Henan extremely persistent heavy rainfall event. *Advances in Atmospheric Sciences*, *40*(3), 350–373. https://doi.org/10.1007/s00376-022-2026-1

Luo, Y., & Du, Y. (2025). Moisture sources and sinks of low-level jets in south China: A backward and forward trace model approach. *Journal of Climate*, *38*(11), 2641–2658. https://doi.org/10.1175/jcli-d-24-0200.1

Luo, Y., Zhang, R., Wan, Q., Wang, B., Wong, W. K., Hu, Z., et al. (2017). The Southern China monsoon rainfall experiment (SCMREX). *Bulletin of the American Meteorological Society*, *98*(5), 999–1013. https://doi.org/10.1175/BAMS-D-15-00235.1

Masutani, M., Woollen, J. S., Lord, S. J., Emmitt, G. D., Kleespies, T. J., Wood, S. A., et al. (2010). Observing system simulation experiments at the National centers for environmental prediction. *Journal of Geophysical Research*, *115*(D7). https://doi.org/10.1029/2009jd012528

Shen, Y., & Du, Y. (2023). Sensitivity of boundary layer parameterization schemes in a marine boundary layer jet and associated precipitation during a coastal warm-sector heavy rainfall event. *Frontiers in Earth Science*, *10*, 1085136. https://doi.org/10.3389/feart.2022.1085136

Skamarock, W. C., Klemp, J. B., Dudhia, J., Gill, D. O., Liu, Z., Berner, J., et al. (2019). A description of the advanced research WRF version 4 [Software]. *NCAR Tech. Note Ncar/Tn-556+ Str*. 145. https://doi.org/10.5065/1dfh-6p97

Sun, J., Zhang, Y., Ban, J., Hong, J. S., & Lin, C. Y. (2020). Impact of combined assimilation of radar and rainfall data on short-term heavy rainfall prediction: A case study. *Monthly Weather Review*, *148*(5), 2211–2232. https://doi.org/10.1175/mwr-d-19-0337.1

Tao, S., & Chen, L. (1987). In C. P. Chang & T. N. Krishnamurti (Eds.), *A review of recent research on the East Asian summer monsoon in China, monsoon meteorology*. Oxford University Press.

Thompson, G., Field, P. R., Rasmussen, R. M., & Hall, W. D. (2008). Explicit forecasts of winter precipitation using an improved bulk microphysics scheme. Part II: Implementation of a new snow parameterization. *Monthly Weather Review*, *136*(12), 5095–5115. https://doi.org/10.1175/2008mwr2387.1

Toth, Z., & Kalnay, E. (1993). Ensemble forecasting at NMC: The generation of perturbations. *Bulletin of the American Meteorological Society*, *74*(12), 2317–2330. https://doi.org/10.1175/1520-0477(1993)074<2317:EFANTG>2.0.CO;2

Weckwerth, T. M., & Parsons, D. B. (2006). A review of convection initiation and motivation for IHOP_2002. *Monthly Weather Review*, *134*(1), 5–22. https://doi.org/10.1175/MWR3067.1

Wei, M., Toth, Z., Wobus, R., & Zhu, Y. (2008). Initial perturbations based on the ensemble transform (ET) technique in the NCEP global operational forecast system. *Tellus A: Dynamic Meteorology and Oceanography*, *60*(1), 62. https://doi.org/10.1111/j.1600-0870.2007.00273.x

Wilks, D. S. (1995). Statistical methods in the atmospheric sciences: An introduction.

Wu, N., Ding, X., Wen, Z., Chen, G., Meng, Z., Lin, L., & Min, J. (2020). Contrasting frontal and warm-sector heavy rainfalls over South China during the early-summer rainy season. *Atmospheric Research*, *235*, 104693. https://doi.org/10.1016/j.atmosres.2019.104693

Xie, P., Joyce, R., Wu, S., Yoo, S.-H., Yarosh, Y., Sun, F., et al. (2019). NOAA climate data record (CDR) of CPC morphing technique (CMORPH) high resolution global precipitation estimates, version 1 [30 min] [dataset]. *NOAA National Centers for Environmental Information*. https://doi.org/10.25921/w9va-q159

Yang, H., Du, Y., Chen, Z., & Fang, J. (2024). Could developing frontal rainfall influence warm-sector rainfall? *Geophysical Research Letters*, *51*(15), e2024GL110430. https://doi.org/10.1029/2024GL110430

Yang, H., Du, Y., & Sun, J. (2025). The merger of a supercell and squall line in the great plains. 1: Initiation of the supercell. *Journal of Geophysical Research: Atmospheres*, *130*(13), e2024JD042393. https://doi.org/10.1029/2024jd042393

Zeng, W., Chen, G., Du, Y., & Wen, Z. (2019). Diurnal variations of low-level winds and precipitation response to large-scale circulations during a heavy rainfall event. *Monthly Weather Review*, *147*(11), 3981–4004. https://doi.org/10.1175/mwr-d-19-0131.1

Zhang, M., & Meng, Z. (2019). Warm-sector heavy rainfall in southern China and its WRF simulation evaluation: A low-level-jet perspective. https://doi.org/10.1175/MWR-D-19-0110.1

Zhang, X., Luo, Y., & Du, Y. (2024). Observation of boundary-layer jets in the northern South China Sea by a research vessel. *Remote Sensing*, *16*(20), 3872. https://doi.org/10.3390/rs16203872

Zhao, J., Guo, J., & Zheng, X. (2024). Impact of multiple radar wind profilers data assimilation on convective scale short-term rainfall forecasts: OSSE studies over the beijing-tianjin-hebei region. *Geoscientific Model Development Discussions*, *2024*, 1–45. https://doi.org/10.5194/gmd-2024-194

Zhao, S., Bei, N., & Sun, J. (2007). Mesoscale analysis of a heavy rainfall event over Hong Kong during a pre-rainy season in South China. *Advances in Atmospheric Sciences*, *24*(4), 555–572. https://doi.org/10.1007/s00376-007-0555-2